Structural Basis for ESCRT-III Protein Autoinhibition

Monika Bajorek[1,2], **Heidi L. Schubert**[1,2], **John McCullough**[1,2], **Charles Langelier**[1], **Debra M. Eckert**[1], **William-May B. Stubblefield**[1], **Nathan T. Uter**[1], **David G. Myszka**[1], **Christopher P. Hill**[1,*], and **Wesley I. Sundquist**[1,*]

[1]Department of Biochemistry, 15 N Medical Drive, Room 4100, University of Utah, Salt Lake City, Utah 84112-5650

Abstract

ESCRT-III (endosomal sorting complexes required for transport-III) subunits cycle between two states: soluble monomers and higher-order assemblies that bind and remodel membranes during endosomal vesicle formation, midbody abscission and enveloped virus budding. Here, we show that the N-terminal core domains of IST1 (increased sodium tolerance-1) and CHMP3 (charged multivesicularbody protein-3) form equivalent four-helix bundles, revealing that IST1 is a previously unrecognized ESCRT-III family member. IST1 and its ESCRT-III binding partner, CHMP1B, both form higher-order helical structures *in vitro*, and IST1-CHMP1 interactions are required for abscission. The IST1 and CHMP3 structures also reveal that equivalent downstream α5 helices can fold back against the core domains. Mutations within the CHMP3 core-α5 interface stimulate the protein's *in vitro* assembly and HIV inhibition activities, indicating that dissociation of the autoinhibitory α5 helix from the core activates ESCRT-III proteins for assembly at membranes.

The ESCRT (<u>e</u>ndosomal <u>s</u>orting <u>c</u>omplexes <u>r</u>equired for <u>t</u>ransport) pathway functions in a series of important membrane remodeling processes, including multivesicular body vesicle formation at endosomal membranes, enveloped virus budding from the plasma membrane, and midbody abscission during cytokinesis (reviewed in 1–4). In performing these functions, ESCRT components cycle between two different states: an inactive state, in which they are dispersed throughout the cytoplasm, and an active state in which they are recruited to specific membranes by upstream adaptor proteins that induce tight membrane binding and component assembly. ESCRT recruitment and assembly ultimately lead to membrane fission, producing endosomal vesicles, budded viruses, or daughter cells. The ESCRT pathway is therefore apparently a mobile machine that can be recruited to different membranes to help mediate membrane remodeling and fission.

---

*Contacts: chris@biochem.utah.edu (CPH), wes@biochem.utah.edu(WIS).
[2]These authors contributed equally to this work.

Most of the ~30 proteins of the human ESCRT pathway function as components of one of five different complexes (termed the ESCRT-0-III and VPS4 complexes). These complexes are recruited sequentially to sites of action, with each successive complex recruiting and activating downstream complexes for membrane association and assembly1–4. Recent studies have revealed that subunits of the late acting ESCRT-III complex can form rings, helical filaments, and tubes *in vitro* and *in vivo*. Thus, ESCRT-III complexes may form "collars" within the cytoplasm-filled necks of membrane vesicles and tubules that can constrict the neck and promote membrane fission5–10. Variants of this general model suggest that one specific subset of ESCRT-III proteins, those of the CHMP4/Snf7p family, may create an encircling ring or spiral, and the other ESCRT-III proteins serve primarily to nucleate and cap the CHMP4/Snf7p filament8–10. ESCRT-III proteins also recruit VPS4 ATPases and induce them to assemble into active complexes. Enzyme recruitment and activation are further promoted by the accessory factors IST1 (Increased Sodium Tolerance-1)11–14 and Vta1p/LIP51–4, both of which can bind ESCRT-III and VPS4 proteins. Once assembled, VPS4 uses the energy of ATP hydrolysis to release the assembled ESCRT-III machinery back into the cytoplasm, thereby allowing multiple rounds of membrane deformation and fission10.

The eleven known human ESCRT-III-like proteins can be divided into seven different families, six of which (CHMP1-6) correspond to the six ESCRT-III-like proteins of *S. cerevisiae*. Most ESCRT-III proteins can form both homo- and hetero-oligomers, and can pair preferentially at membrane sites of action (e.g., CHMP4-CHMP6 and CHMP2-CHMP3)6,15. ESCRT-III proteins vary significantly in primary sequence, but all share common N-terminal core domains of ~150 residues. The core domain of one ESCRT-III protein, $CHMP3_{8-183}$, has been crystallized and shown to form a four-helix bundle16. The longer first two helices form an extended hairpin, and the shorter two helices pack at the open end of the hairpin. Sequences located beyond the helical core exhibit autoinhibitory activities, and there is now considerable biochemical and genetic evidence that these downstream sequences prevent premature membrane binding and assembly6,16–21. Downstream sequence elements also bind a variety of different late-acting ESCRT factors, including ALIX22 and a series of MIT domain-containing proteins and enzymes such as ubiquitin hydrolases (e.g., AMSH and UBPY)23,24, proteases (calpain 7)25,26, ATPases (Spastin and VPS4 proteins)21,27–30, and ATPase activators (Vta1p/LIP5)31–33. Different ESCRT-III subunits exhibit distinct binding partner specificities, which helps rationalize the need for so many different ESCRT-III proteins.

IST1 is a recently identified, late-acting ESCRT pathway factor that binds LIP5/Vta1p, VPS4 and CHMP1/Did2p11–14. The precise function(s) of IST1 are not yet well understood and, indeed, IST1 can exert both positive11–14 and negative12 effects on ESCRT pathway functions. Yeast Ist1p exhibits synthetic interactions with the Vta1p-Vps60p (LIP5-CHMP5) complex in endosomal protein sorting reactions, implying that Ist1p functions in MVB vesicle formation, albeit in a non-essential role12,13. Human IST1 localizes to midbodies, and its depletion inhibits abscission but not HIV budding11,14. IST1 proteins therefore appear to play important roles in cytokinesis, auxiliary roles in endosomal protein sorting, and no essential role in HIV budding. Biochemical and secondary structure analyses indicate

that IST1 is composed of a helical N-terminal domain (residues 1–189, here termed IST1$_{NTD}$, but also called the "ELYC" domain after a conserved tetrapeptide sequence12), C-terminal <u>M</u>IT <u>I</u>nteracting <u>M</u>otifs (MIM) that can bind cooperatively to the MIT domains of VPS4 enzymes (321–366)11,14, and a central linker region that is predicted to lack persistent secondary structure (~190–320)11,14.

Extensive structural and biochemical analyses have revealed many of the relevant molecular interactions that allow different ESCRT components to associate with one another, with PI(3)P-containing membranes, and with ubiquitylated protein cargoes1–4. In contrast, the mechanisms that regulate ESCRT pathway assembly and disassembly are much less well understood. Here, we have determined crystal structures of human IST1 and CHMP3 proteins, and performed complementary biochemical analyses that characterize the functional importance of the IST1-CHMP1 binding interaction in cytokinesis and suggest how ESCRT-III proteins can switch between their inactive, soluble states and their active, membrane-bound assemblies.

RESULTS

Characterization of recombinant CHMP3 and IST1 proteins

We developed methods for expressing and purifying recombinant human IST1 and CHMP3 proteins for structural and biochemical studies. Full length CHMP3 and an N-terminally truncated construct (CHMP3$_{8–222}$) were both monomeric in solution as analyzed by equilibrium sedimentation (Fig. 1), in good agreement with a previous report16. Full length IST1 was also monomeric under high ionic strength conditions (>300 mM NaCl)11, but aggregated at lower ionic strength. The purified N-terminal domain of IST1 (IST1$_{NTD}$, residues 1–189) behaved like the full-length protein in that it was also monomeric under high ionic strength conditions (Fig. 1c) and insoluble in lower ionic strength solutions. This construct was particularly amenable for structural and biochemical studies, presumably because it lacked the proline-rich linker region present in the full-length protein.

Crystal structures of IST1$_{NTD}$

We crystallized IST1$_{NTD}$ under high ionic strength conditions, and the structure was determined in space groups P2$_1$ (1.8 Å resolution) and P4$_3$2$_1$2 (2.6 Å, Table 1 and Supplementary Fig. 1a,b). The structures were similar, and the higher resolution P2$_1$ structure is described here. IST1$_{NTD}$ is composed of eight helices, which pack to create a flat, elongated structure, with overall dimensions of $21 \times 30 \times 60$ Å (Fig. 2a). The two longest helices, α1 and α2, form a helical hairpin that packs against the smaller α3 and α4 helices to create an asymmetric four-helix bundle (termed the "core"). Beyond the core, the segment between helices α4 and α5 forms a flap that tracks along the length of the molecule, packing against the α2/α3 edge. The flap contains two short helices, which are designated αA and αB in order to maintain a consistent numbering scheme for conserved ESCRT-III helices. α5 packs perpendicularly across α1 and α2 near the closed end of the hairpin and is termed the "autoinhibitory helix". A final turn takes the polypeptide across the hairpin loop and into α6, which projects away from the core. This helix was only seen in the P2$_1$ crystal form where it is stabilized by lattice contacts. As discussed below, the IST1$_{NTD}$

structure appears to represent a closed/autoinhibited ESCRT-III conformation in which the flap and autoinhibitory helix fold against the core to prevent higher order interactions.

$IST1_{NTD}$ bears an unexpected resemblance to the published $CHMP3_{8-183}$ structure16 (Figs. 2a–c), and the four helices of the $IST1_{NTD}$ core superimpose with the first four helices of CHMP3 with an RMSD of 2.4 Å (128 Cα positions). Muziol *et al*. noted that the α1 edge of CHMP3 is distinctly cationic and proposed that this surface binds membranes16. The equivalent IST1 surface is also basic, although the α3/α4 face is even more so (Figs. 2d–f).

In addition to their similar core structures, the autoinhibitory α5 helices of $CHMP3_{8-183}$ and $IST1_{NTD}$ sit in equivalent positions (α5, orange). Thus, all of the ordered helices in the $CHMP3_{8-183}$ structure have analogs in $IST1_{NTD}$. However, the assigned connectivity of the autoinhibitory helices differ between the two structures because this helix is connected in "cis" to the $IST1_{NTD}$ core via the flap segment, whereas it was assigned to an adjacent molecule in the $CHMP3_{8-183}$ lattice16. Muziol *et al*. noted, however, that the $CHMP3_{8-183}$ connectivity could not be defined unambiguously owing to a lack of visible electron density for the flap region16. We therefore speculate that the $CHMP3_{8-183}$ connectivity may actually match that of $IST1_{NTD}$ and that the $CHMP3_{8-183}$ structure may also represent a closed conformation.

Crystal structures of CHMP3

The $CHMP3_{8-183}$ construct lacked the final 39 CHMP3 residues, which may have favored an open conformation16. We therefore attempted to remove this ambiguity by crystallizing both the full-length monomeric $CHMP3_{1-222}$ protein and a slightly truncated $CHMP3_{8-222}$ protein. Both proteins crystallized isomorphously in space group $P2_1$, but $CHMP3_{8-222}$ diffracted to slightly higher resolution (4.0Å), and this structure is therefore reported (Fig. 2c and Table 1). The $CHMP3_{8-222}$ structure was determined by molecular replacement using the core of $CHMP3_{8-183}$ as a search model and then subjected to rigid body refinement. Discernible features beyond the search model were limited, but the structure solution is supported by the molecular replacement statistics (Methods) and by unbiased electron density maps (Supplementary Fig. 2). In addition to the four core helices, density for the autoinhibitory helix was evident in unbiased electron density maps, particularly for one of the two independent molecules in the asymmetric unit (Supplementary Fig. 2c,d). Although the connectivity between α4 and α5 was not defined by experimental electron density, α5 appears to sit in the same position in both the $CHMP3_{8-183}$ and $CHMP3_{8-222}$ structures despite different crystal packing interactions in the two lattices. We have connected α4 and α5 in cis rather than in trans to create a structure with the same topology as $IST1_{NTD}$, and this assignment is consistent with biochemical analyses described below.

Finally, we reasoned that a construct corresponding to the CHMP3 core alone could not adopt an autoinhibited conformation and might therefore reveal authentic protein-protein interactions used for ESCRT-III assembly. The CHMP3 core construct ($CHMP3_{1-150}$) was crystallized in space group $P6_1$ and the structure solved by molecular replacement (3.7 Å resolution, Table 1 and Supplementary Fig. 2b). As expected, the $CHMP3_{1-150}$ core was very similar to the cores of the other CHMP3 and $IST1_{NTD}$ structures, although, as described below, the lattice interactions were unique.

Crystal packing interactions

We analyzed lattice contacts in the different IST1 and CHMP3 crystal structures to determine whether they were strong candidates for authentic interactions used in ESCRT-III protein assembly (see Supplementary Fig. 3 for a complete catalog of the different lattice interactions). Overall, there are not compelling reasons to believe that any of the various crystal contacts represent authentic assembly interfaces. Moreover, both of our CHMP3 structures lacked the "side-to-side" dimer interface seen in the $CHMP3_{8-183}$ structure[16] and postulated as a possible ESCRT-III assembly interface[6,7].

Two of the new CHMP3 interfaces merit comment because they are mediated by a conserved, exposed hydrophobic surface on the closed "tip" of the $\alpha1/\alpha2$ hairpin. In the $CHMP_{8-222}$ structure, two adjacent molecules associate through a small (359 Å^2) two-fold symmetric "tip-to-tip" dimer interface (Fig. 3a,b). A similar tip-to-tip interface was also present in the $CHMP3_{8-183}$ lattice[16], and this is the only interface that has been seen in more than one crystal form.

A different type of tip-to-tip interaction is present in the $CHMP3_{1-150}$ lattice. In this case, the interaction lacks two-fold rotational symmetry and instead follows a crystallographic 3_1 screw axis that creates an infinite $CHMP3_{1-150}$ filament with interfaces on both sides of the tip (Fig. 3c–e). The yeast homolog of CHMP3 (Vps24p) can assemble into three-stranded filaments *in vitro*[7], although the relationship between the Vps24p filaments and the crystallographic CHMP3 filaments remains to be determined. In summary, the crystal packing interactions in our IST1 and CHMP3 structures do not obviously correspond to authentic biological interfaces, but do reinforce the idea that the exposed hydrophobic surface located at the tip of the helix 1/2 loop is a preferred site for protein-protein interactions[6,7,16].

$IST1_{NTD}$ binds CHMP1 proteins

Many ESCRT-III proteins bind one another, and previous studies have shown that the N-terminal domain of IST1 binds preferentially to the C-terminal region of the CHMP1 subset of ESCRT-III proteins[11–14]. To map the IST1 binding surface more precisely, we created an ensemble of IST1 proteins with point mutations at conserved, surface-exposed residues and tested them for CHMP1A and CHMP1B interactions using: 1) immunoprecipitation (IP) reactions in 293T cells (not shown), 2) GST-pulldown experiments with recombinant proteins (not shown), and 3) biosensor binding experiments in which pure recombinant CHMP1B bound immobilized GST-$IST1_{NTD}$ (Fig. 4).

As shown in Fig. 4a,b, CHMP1B bound wild type $IST1_{NTD}$ with an estimated dissociation constant of 22 ± 2 μM. CHMP1B binding was unaltered by most mutations tested, including mutations within the closed tip of the $\alpha1/\alpha2$ hairpin (e.g., E39A, Y43D, K48D, R51D, I54D and R55D), and in the $IST1_{NTD}$ surface that corresponded to the "side-to-side" dimer interface seen in the crystal structure of $CHMP3_{8-183}$ and included the signature $_{73}E\underline{L}YCE\underline{L}_{78}$ motif (e.g., E70A, $\underline{L}$74R, Y75A, and $\underline{L}$78R). However, one mutation along helix 2 (E67A) reduced CHMP1B binding in the IP and pulldown experiments and lowered the CHMP1B binding affinity six-fold in the biosensor binding assay, suggesting

that this residue contributed to the CHMP1B binding site. Mutations in adjacent surface exposed residues were therefore tested to identify the CHMP1B binding site more precisely, and these analyses revealed three IST1 mutants that bound CHMP1B weakly (>8-fold affinity reductions, IST1$_{Y64D}$, IST1$_{Y165A}$ and IST1$_{E168R}$), three IST1 mutants that bound CHMP1B with intermediate affinities (2- to 8-fold reductions, IST1$_{D63A}$, IST1$_{E67A}$ and IST1$_{R164D}$), and one mutation that still bound strongly to CHMP1B (IST1$_{E163R}$, data not shown).

Given the proximity of the apparent CHMP1B binding site to the IST1 autoinhibitory helix α5, we also tested the effects of a series of IST1 mutations predicted to destabilize the α5-core interface (V56D, I60D, L166D, and I169D). All of these IST1 mutations blocked CHMP1B binding entirely (not shown), indicating that CHMP1B binds the closed conformation of IST1$_{NTD}$ seen in the crystal structures. As summarized in Fig. 4c, mutations that inhibited CHMP1B binding clustered within or near a groove created by packing of autoinhibitory helix α5 against core helix α2. The groove features a pair of exposed Tyr residues (Tyr64 and Tyr165), which likely contribute to CHMP1B binding.

The IST1-CHMP1B interactions function in cytokinesis

To determine whether CHMP1 binding was necessary for IST1 cytokinesis function(s), we tested whether IST1 mutations that impaired CHMP1B binding also inhibited abscission. Depletion of endogenous IST1 increased the percentage of HeLa cells with visible midbodies from 4±1% to 20±3% (Fig. 5a, compare lanes 1 and 2 and Fig. 5b, panels 1 and 2), and this midbody arrest defect was largely (though not entirely) rescued by re-expression of a wild type, siRNA-resistant IST1 construct (8±2%, lane/panel 3)[11]. Midbody arrest was also corrected by an IST1 protein with a mutation in the tip of the α1/α2 hairpin that retained strong (S) CHMP1B binding (IST1$_{R51D}$, 8±1%, lane/panel 4). In contrast, three weak-binding IST1 mutants failed to rescue midbody arrest (18–21%, Fig. 5a, lanes 7–9 and Fig. 5b, panels 5 and 6). Point mutations within the α5-core interface that blocked CHMP1B binding also blocked rescue of the midbody arrest defect. However, these mutant proteins partitioned almost exclusively into the insoluble/membrane-bound cellular fractions, and their failure to support abscission may therefore reflect either aberrant CHMP1 binding or IST1 protein mislocalization (see Supplementary Fig. 4 and the Supplementary Discussion). Finally, two IST1 mutants with intermediate (I) CHMP1B binding affinities rescued midbody arrest to an intermediate extent (12–13%, Fig. 5a lanes 5 and 6). Hence, there was an excellent correlation between the ability of different IST1 constructs to bind CHMP1B *in vitro* and to function in abscission, indicating that CHMP1 binding is required for IST1 abscission function(s).

IST1$_{NTD}$ and CHMP1B form homopolymeric helices *in vitro*

CHMP3 can co-polymerize with truncated CHMP2A proteins to form 50 nm diameter helical tubes *in vitro*[6]. As noted above, both IST1 and IST1$_{NTD}$ became insoluble under low ionic strength conditions, and we therefore tested whether these proteins assembled into regular structures. Assembly conditions were initially surveyed using light scattering to follow complex formation. As shown in Fig. 6a, monomeric IST1$_{NTD}$ spontaneously polymerized into high molecular weight complexes that strongly scattered light at 330 nm

when the protein was diluted from a high salt buffer (350 mM NaCl) into a low salt buffer (100 mM NaCl). In contrast, $IST1_{NTD}$ did not scatter light when diluted into an otherwise equivalent high salt buffer (350 mM NaCl).

EM analyses revealed that the light scattering $IST1_{NTD}$ assemblies were large tubular structures with diameters of ~700 nm (Fig. 6b, lower left panels). The tubes appeared to be open along one edge and may therefore be curled sheets rather than fully closed helices. Lattice lines were evident in some assemblies, and the clearest lattice spacing was ~440 Å, which presumably represents a supermolecular spacing because the maximal length of a single $IST1_{NTD}$ molecule is only ~60 Å. As noted above, CHMP3 interactions can be mediated by various different kinds of tip-to-tip interactions (refs. 6,7 and Fig. 3). A series of three different point mutations in the analogous IST1 surface (Y43D, R51D and I54D) also inhibited $IST1_{NTD}$ polymerization (Fig. 6a,b. right column), and see Supplementary Fig. 5 for ESCRT-III protein alignments). $IST1_{NTD}$ assembly therefore likely also requires some type of tip-to-tip interaction.

We also attempted to test whether $IST1_{NTD}$ and CHMP1B could co-polymerize like the $CHMP2A_{9-161}$-CHMP3 pair6. However, controls for these experiments revealed that pure recombinant CHMP1B alone polymerized into helical tubes when diluted into low salt buffers, even in the absence of $IST1_{NTD}$ (Fig. 6c). CHMP1B tubes were of intermediate size (~230 nm in diameter), appeared to be fully closed, and had visible lattice spacing of ~420 Å, which were similar to the lattice spacing in the $IST1_{NTD}$ tubes. Thus, both $IST1_{NTD}$ and CHMP1B, like CHMP2A-CHMP36, form tubular structures *in vitro*, and the ability to assemble into helical tubes therefore appears to be a property common to many ESCRT-III core domains. However, the IST1 and CHMP1B tubes were homopolymeric, and were significantly larger than those formed by CHMP2A-CHMP3 heteropolymers6.

Mutations at the tip of the CHMP3 α1/ α2 hairpin inhibit CHMP2A binding

Like the IST1-CHMP1 pair, CHMP2A and CHMP3 bind one another preferentially. To investigate this interaction further, we used GST pulldown assays to test for binary interactions between CHMP2A and GST-CHMP3 (Figs. 7a,b). These experiments were performed at low protein concentrations where higher order assemblies were not detectable (35μM CHMP2A, ~7 μM GST-CHMP3). CHMP2A protein bound GST-CHMP3 (Fig. 7b, lane 3) but did not bind a matrix control (lane 2). CHMP2A also bound the truncated GST-$CHMP3_{1-150}$ protein (lane 4), indicating that CHMP2A interacted with the CHMP3 core and that the binary interaction was not dramatically affected by removal of the terminal CHMP3 autoinhibitory sequences. In contrast, a double point mutation (V59D, V62D) that disrupted the exposed hydrophobic surface on one side of the tip of the CHMP3 α1/ α2 hairpin eliminated CHMP2A binding (lane 5). These data suggest that CHMP2A and CHMP3 interact through a tip-to-tip type interaction, and demonstrate that the binary CHMP2A-CHMP3 and IST1-CHMP1B pairs interact via different binding surfaces and therefore form structurally distinct complexes.

Autoinhibitory helix interface mutations activate CHMP3 for polymerization

Comparative analyses of the $IST1_{NTD}$, $CHMP3_{8-183}$, and $CHMP3_{8-222}$ structures suggested a model for ESCRT-III autoinhibition in which the $\alpha 5$ helix and flap elements fold back against the protein core to prevent higher order assembly. We tested this idea by introducing destabilizing mutations within the $\alpha 5$-core interface of the full length CHMP3 protein and testing their effects on CHMP2A co-assembly. Although the full length CHMP2A and CHMP3 proteins bind one another, these two proteins do not readily form higher order helical assemblies (Fig. 7c, panel 1, and see ref. 6). In contrast, a $CHMP3_{1-150}$ protein that lacked the flap and autoinhibitory helix readily copolymerized with CHMP2A to form long, regular helical tubes (Fig. 7c, panel 2, positive control). Since CHMP2A forms binary complexes with both CHMP3 and $CHMP3_{1-150}$, these experiments imply that CHMP3 residues 151–222 inhibit additional interaction(s) required for higher order assembly.

To examine the mechanism of CHMP3 autoinhibition, we mixed full length CHMP2A with full-length CHMP3 proteins that contained mutations on either side of the core-$\alpha 5$ interface ($CHMP3_{V48D, A64D}$ and $CHMP3_{I168D, L169D}$, see Fig. 7a). Both sets of mutations activated CHMP3 for assembly, as reflected in the formation of numerous rings, tubes, and cones (Fig. 7c, panels 3 and 4). The tubes were similar in diameter to those formed in the $CHMP2A/CHMP3_{1-150}$ control reaction (~50 nm) but were typically shorter, possibly because the point mutations activated CHMP3 proteins less fully than removal of the entire autoinhibitory region.

We also tested whether the binary CHMP2A-CHMP3 interface detected at low protein concentrations was required for higher order assembly. As expected, mutations on either side of the CHMP3 autoinhibitory interface did not significantly affect CHMP2A binding to GST-CHMP3 ($CHMP3_{V48D, A64D}$ and $CHMP3_{I168D, L169D}$, Fig. 7b, lanes 6 and 7). However, a CHMP3 protein carrying mutations in both the tip and autoinhibitory interfaces ($CHMP3_{V59D, V62D, I168D, L169D}$) could neither bind CHMP2A in the GST pulldown assay (Fig. 7b, lane 8) nor assemble into helical tubes (Fig. 7c, panel 5). These experiments imply that tip-to-tip interactions contribute to CHMP2-CHMP3 co-assembly, in good agreement with a previous study6.

Mutations in the autoinhibitory helix activate CHMP3 *in vivo*

Although co-expression of full length CHMP3 has only minimal effects on HIV-1 budding, truncated CHMP3 constructs lacking C-terminal autoinhibitory elements potently inhibit virus budding, presumably because the activated protein sequesters itself and other ESCRT-III proteins on cellular membranes20. Inhibition of HIV release therefore provides a sensitive assay for CHMP3 activation *in vivo*. We used this system to examine whether mutations in the $\alpha 5$-core interface also activate CHMP3 *in vivo*. As shown in Fig. 8, co-overexpression of full length CHMP3 with an HIV-1 vector system had little effect on the release of viral particles, as measured by the levels of virion-associated CA proteins released from 293T cells (Fig. 8, panel 3, compare lanes 1 and 2) or by viral titers (panel 4, compare lanes 1 and 2). In contrast, HIV release and infectivity were potently inhibited by co-expression of a CHMP3 protein that lacked the autoinhibitory region entirely ($CHMP3_{1-150}$, positive control, compare lanes 2 and 4, >250-fold infectivity reduction). In the actual

experiment, two different CHMP3 proteins with point mutations within the α5-core interface (CHMP3$_{I168D, L169D}$ and CHMP3$_{V48D, I168D, L169D}$) reduced HIV vector release and infectivity by 1.7- and 3-fold, respectively (compare lanes 4 and 5 to lane 2). Western blots confirmed that the full-length CHMP3 proteins and viral Gag proteins and proteolytic processing products were expressed at similar levels (panels 1 and 2, respectively). Thus, point mutations in the α5-core interface enhanced the ability of CHMP3 proteins to inhibit HIV-1 budding *in vivo*, although this enhancement was much weaker than that seen upon deletion of the entire autoinhibitory region. We presume that the weaker effects seen for the point mutants reflects either incomplete activation and/or their ability to interact with VPS4 which will reduce their propensity to become "trapped" on membranes as compared to CHMP3$_{1-150}$ (which lacks a terminal VPS4 binding site).

DISCUSSION

Our studies have unexpectedly revealed that the N-terminal domain of IST1 contains an asymmetric four-helix bundle that closely resembles the core of the ESCRT-III protein, CHMP3 (Fig. 2). Like other ESCRT-III proteins, IST1 also: 1) localizes to midbodies and functions in cytokinesis[11,14] and MVB vesicle sorting[12,13], 2) binds preferentially to another subset of ESCRT-III proteins (the CHMP1 proteins)[11–14], 3) contains MIM elements near its C-terminus that can bind VPS4 and LIP5 MIT domains[11,14], and 4) can self-assemble into tubular structures *in vitro* (Fig. 6). Thus, despite its larger size and primary sequence divergence, IST1 is an ESCRT-III protein family member.

Despite these similarities, there are also important differences between IST1 and CHMP3, particularly in the binary interactions that they make with their CHMP1 and CHMP2 binding partners. Our mutational analyses mapped the CHMP1 binding site to a groove formed by the autoinhibitory α5 helix and the core α2 helix of IST1$_{NTD}$ (Fig. 4). CHMP1B binding was also inhibited by mutations expected to favor the (hypothetical) open IST1$_{NTD}$ conformation, implying that CHMP1 binds the closed conformation seen in our IST1$_{NTD}$ crystal structures (Fig. 2). IST1 mutations that blocked CHMP1B binding also prevented IST1 from functioning in abscission, implying that these two protein proteins must act together during this final stage of cytokinesis (Fig. 5). In contrast, binary interactions between CHMP2 and CHMP3 were not inhibited by mutations that displaced or even removed the α5 helix entirely (Fig. 7). This interaction was sensitive to mutations at the tip of the α1/α2 hairpin, however, suggesting that unlike IST1 and CHMP1B, CHMP2 and CHMP3 likely interact through some sort of a tip-to-tip interaction (Fig. 7).

In vitro assemblies formed by ESCRT-III proteins include filaments, rings, cones, curled sheets, and tubes (Figs. 6b,c, Fig. 7c and refs. 6,7). At present, we do not know which (if any) of these different *in vitro* assemblies mimic different ESCRT-III assemblies formed *in vivo*. As noted previously[5–7], however, filaments, rings and/or tubes could correspond to "collars" within the necks of budding particles, and tapered tubes/spiraling cones could provide a mechanism for closing the neck during budding[6] (see Fig. 7c, structure types 3). Although the precise molecular interactions that mediate higher order ESCRT-III assembly remain to be determined, both IST1$_{NTD}$ and CHMP2-CHMP3 assemblies are inhibited by point mutations within the conserved, exposed hydrophobic surface located at the tip of the

α1/α2 hairpin (Fig. 6b, Fig. 7c), suggesting that some type of tip-mediated interface forms within both assemblies. Two distinct types of homopolymeric ESCRT-III tip-to-tip interactions have now been seen crystallographically (ref. 16 and Fig. 3), and a third type was inferred from cryo-EM studies of helical yeast Vps24/CHMP3 assemblies[7]. Thus, the conserved hydrophobic surface at the tip of ESCRT-III proteins is a preferred interaction site, although it is not yet clear which, if any, of the tip-to-tip interactions characterized to date represent biologically relevant interactions. We also note that although the IST1 R51D tip mutation inhibits IST1 assembly (Fig. 6a,b) it does not block the ability of IST1 to function in cytokinesis (Fig. 5), implying different requirements for IST1 assembly *in vitro* and abscission function *in vivo*. Finally, in addition to tip contacts, at least one more protein-protein interface is required to create two-dimensional surfaces in helices or sheets. These secondary interaction(s) are disfavored by C-terminal autoinhibitory interactions (ref. 6 and this work), and may correspond to one of the several different kinds of higher order packing interactions that have been proposed on the basis of cryo-EM analyses of helical ESCRT-III protein assemblies[6,7].

Our IST1$_{NTD}$ structure revealed that the downstream flap and autoinhibitory helix can fold back against the ESCRT-III core, and this topology was unambiguously established by high quality electron density throughout the flap region (Fig. 2 and Supplementary Fig. 1). Analogous models can be built for the CHMP$_{8-183}$ and CHMP3$_{8-222}$ structures, although in those cases the connectivity has not been established unambiguously. Nevertheless, we suggest that all of these structures likely correspond to the closed, autoinhibited ESCRT-III conformation because: 1) both IST1$_{NTD}$ and CHMP3$_{8-222}$ are monomers in solution under the conditions used for crystallization (although IST1$_{NTD}$ polymerizes under low salt conditions) (Fig. 1), 2) IST1 is redistributed into the insoluble membrane-bound/assembled fractions of cellular extracts by mutations that disrupt core packing of the autoinhibitory elements (Supplementary Fig. 4), 3) CHMP3 and CHMP2A can be activated for co-assembly by deletions that remove the autoinhibitory helices from CHMP2A6 or CHMP3, or by point mutations that destabilize packing of the CHMP3 autoinhibitory helix against the core (Fig. 7), and 4) mutations that remove the autoinhibitory helix or destabilize its core packing interactions render CHMP3 a dominant inhibitor of HIV-1 budding (refs. 17,20 and Fig. 8). Nevertheless, there is also good evidence that additional contacts beyond those visualized in our IST1$_{NTD}$ or CHMP3 structures help to stabilize the closed CHMP3 conformation even further because point mutations in the autoinhibitory helix-core interface do not activate CHMP3 to the same extent as does deletion of the entire autoinhibitory region (Fig. 7c and Fig. 8) and because short C-terminal deletions downstream of the autoinhibitory α5 helix can also enhance ESCRT-III membrane binding and inhibition of HIV-1 budding, albeit to a lesser extent than deletions that include α5[17,20]. These observations indicate that the terminal ESCRT-III helix 6 (and possibly also flap sequences) make energetically important contacts that favor the closed ESCRT-III conformation.

In summary, many ESCRT-III proteins can adopt two distinct conformational states[6,16–21], and our studies provide a molecular model for the closed, monomeric state adopted by ESCRT-III proteins when they are distributed throughout the cytoplasm (or loosely associated with non-specific membranes)[34]. Primary sequence and secondary structure

analyses indicate that all ESCRT-III proteins have analogous α5 helices in equivalent positions, and the mechanism of autoinhibition described here is probably quite general (see Supplementary Fig. 5a). Surrounding elements can vary significantly in sequence, length, and secondary structure, however, and likely mediate a variety of different protein-protein interactions33. Interestingly, these different protein-protein interactions can be enhanced, inhibited, or unchanged by mutations that favor the open states of various ESCRT-III proteins (e.g., refs. 21,22,28,33). Thus, changes in protein-protein and protein-membrane interactions that accompany ESCRT-III activation and assembly are likely to reflect the conformational changes described here, coupled with avidity effects created by the assembly of oligomeric ESCRT-III protein arrays.

METHODS

Expression vectors and antibodies

Vectors and antibodies are summarized in Supplementary Table 1 and Supplementary Table 2.

Protein expression and purification

We expressed IST1 and CHMP proteins in *E. coli* with N-terminal GST affinity tags. Protein expression, purification, and tag removal are described in the Supplemental Methods.

Equilibrium sedimentation analyses

We centrifuged purified CHMP3, CHMP3$_{8-222}$, and IST1$_{NTD}$ in 10 mM Tris-HCl pH 8.0, 100mM NaCl (CHMP3 proteins) or 50 mM Tris-HCl pH 7.0, 350 mM NaCl, and 1 mM DTT (IST1$_{NTD}$) at 4°C in an Optima XL-A centrifuge (Beckman). Initial protein concentrations are given in Fig. 1a–c. Data were collected after equilibrium was obtained at two speeds (20,000 and 24,000 rpm) and the molecular masses were determined from the resulting six data sets for each protein by globally fitting to single ideal species models using the nonlinear least-squares algorithms in the Heteroanalysis software38. Protein partial specific volumes and solvent densities were calculated with the program SEDNTERP (version 1.09)39.

Protein crystallization and data collection

We crystallized IST1$_{NTD}$, CHMP3$_{8-222}$ and CHMP3$_{1-150}$ by vapor diffusion at 13°C. IST1$_{NTD}$ crystals grew from a 12 mg ml^{-1}solution in gel filtration buffer. Crystal form I (diamond-shaped morphology, P4$_3$2$_1$2, one molecule per asymmetric unit (AU)) grew in 1–3 days by simple dehydration of a 2 μl drop. Crystals were cryoprotected by passage through silica oil, suspended in a nylon loop and plunged into liquid nitrogen. Crystal form II (rods/plates, P2$_1$, one molecule per AU) grew from a 1:1 v/v mixture of protein and well solution (180 mM KCl, 50 mM HEPES, pH 7.6, 35% pentaethritol propexylate and 7% v/v ethylene glycol). Crystals were cryocooled directly without solution modification. Native data for both crystal forms were collected on a Rigaku Micromax 007HF rotating anode generator equipped with VeriMax-HR optics.

$CHMP3_{8-222}$ crystals (flat plates, $P2_1$, two molecules per AU) grew from grew from a 1:2 v:v mixture of protein (30 mg ml^{-1} in gel filtration buffer) and well solution (10–22% PEG 6000 and 0.1M Na HEPES, pH 7.0–8.0). Data were collected at SSRL beamline 11–1. $CHMP3_{1-150}$ crystals (hexagonal rods, $P6_1$) grew from a 1:1 v/v mixture of protein (22mg ml^{-1} in gel filtration buffer) and well solution (16% v/v PEG 3350, 0.1 M Na HEPES, pH 7.0–8.0, 200 mM proline). Data were collected on a rotating anode generator. Despite extensive effort, we were unable to collect better data at the synchrotron. Data were indexed and scaled with the program HKL200040 (Table 1).

Structure determinations

Three-wavelength MAD data were collected from selenomethionine-substituted $IST1_{NTD}$ at SSRL beamline 9–1 to 3.4 Å. Three of the six potential selenium sites were identified using SOLVE41, and the resulting 4.0 Å phases were solvent flattened and extended to 2.6 Å resolution using the native data and the program DM42. The four core helices (α1–4) were built using O43, and this partial model was used for molecular replacement determination of the higher resolution form II crystal structure using PHASER44. The models were completed with COOT45, refined with REFMAC546, and analyzed using programs within the CCP4 suite47. The similar $IST1_{NTD}$ structures in the two crystal forms overlapped with a root mean square deviation (RMSD) of 1.25 Å on $C\alpha$ atoms 12–170.

Both CHMP3 structures were determined by molecular replacement using the published $CHMP3_{8-183}$ structure (pdb code 2GD516) as the search model. The correctness of the solutions is supported by PHASER44 Z-scores of 9.1 ($CHMP3_{8-222}$) and 8.6 ($CHMP3_{1-150}$) and by the appearance of electron density when portions of the search model were omitted from the molecular replacement calculation (Supplementary Fig. 2). Both structures are hampered by low resolution and a correspondingly low number of unique reflections. Rfree sets of 5% contain too few reflections (~120) to be statistically useful. An optimal strategy was therefore determined by considering Rfree values from multiple refinement runs, each starting from the same molecular replacement solution and with a different small number (~200) of reflections in the test set. This indicated that the best results were obtained using rigid-body refinement in PHENIX35, with each helix treated as a rigid unit. This approach was therefore applied to the starting molecular replacement solution but using all of the reflections in the calculation (no test set).

Biosensor binding assays

We used BIACORE2000 and 3000 instruments (GE Healthcare) to measure the binding of pure recombinant CHMP1B to immobilized GST-$IST1_{NTD}$ proteins captured from *E. coli* extracts28 as described in Supplemental Methods.

IST1 depletion and rescue experiments

We transfected HeLa-M cells with IST1 expression vectors (1 μg/well, Lipofectamine 2000, Invitrogen) and siRNA (20nM, Lipofectamin RNAi MAX, Invitrogen) following the time course: t=0, seed cells in DMEM/10% FCS (six well plates, 4×10^5 cells per well (t=0 h); t=24 h, IST1 expression vector; t=32 h, media change + IST1 vector; t=44 h, trypsin treat and reseed on 18 mm glass cover slips for immunofluorescence analyses (3×10^4 cells per

cover slip) and in 6 well plates for western blotting (3×10^5 cells per well); t=56 h, media change + siRNA; t=68 h, media change + siRNA; t=94 h, fix or harvest cells and analyze.

Direct visualization of cytokinesis defects

We fixed transfected HeLa-M cells with 4% paraformaldehyde and stained with SYTOX-Green (Invitrogen) and with mouse anti-α-Tubulin and a secondary Alexa 594-conjugated goat anti-mouse antibody. We scored midbody arrest manually for 3 blinded sets of 200 cells by direct visualization using fluorescence microscopy.

ESCRT-III assembly reactions

Assembly conditions for IST1$_{NTD}$, CHMP1B and CHMP2A/CHMP3 proteins are provided in the Supplemental Methods.

Transmission electron microscopy

We analyzed assembly reactions using TEM with negative staining. Carbon-coated grids were placed on aliquots of each assembly reaction (7μl, 90 sec), washed with 3–4 drops of 0.1M KCl, stained with 3–4 drops of 4% uranyl acetate, air dried, and imaged (Hitachi 7100 TEM).

GST pulldown assays

We tested the binding of pure recombinant CHMP2A proteins to various GST-CHMP3 proteins as described in the Supplemental Methods.

HIV-1 vector release and infectivity

We co-transfected 293T cells with vectors expressing CHMP3-Myc and HIV-1 and harvested supernatants and cells after 24 h, Western blotting was used to analyze cellular proteins and virions pelleted through 20% sucrose cushion and HeLa-M cell transduction to measure vector titers. Full details are provided in Supplemental Methods.

Supplementary Material

Refer to Web version on PubMed Central for supplementary material.

Acknowledgements

REFERENCES

1. Hurley JH. ESCRT complexes and the biogenesis of multivesicular bodies. Curr Opin Cell Biol. 2008; 20:4–11. [PubMed: 18222686]

2. Williams RL, Urbe S. The emerging shape of the ESCRT machinery. Nat Rev Mol Cell Biol. 2007; 8:355–368. [PubMed: 17450176]

3. Saksena S, Sun J, Chu T, Emr SD. ESCRTing proteins in the endocytic pathway. Trends Biochem Sci. 2007; 32:561–573. [PubMed: 17988873]

4. Piper RC, Katzmann DJ. Biogenesis and function of multivesicular bodies. Annu Rev Cell Dev Biol. 2007; 23:519–547. [PubMed: 17506697]

5. Hanson PI, Roth R, Lin Y, Heuser JE. Plasma membrane deformation by circular arrays of ESCRT-III protein filaments. J Cell Biol. 2008; 180:389–402. [PubMed: 18209100]

6. Lata S, et al. Helical structures of ESCRT-III are disassembled by VPS4. Science. 2008; 321:1354–1357. [PubMed: 18687924]

7. Ghazi-Tabatabai S, et al. Structure and disassembly of filaments formed by the ESCRT-III subunit Vps24. Structure. 2008; 16:1345–1356. [PubMed: 18786397]

8. Teis D, Saksena S, Emr SD. Ordered assembly of the ESCRT-III complex on endosomes is required to sequester cargo during MVB formation. Dev Cell. 2008; 15:578–589. [PubMed: 18854142]

9. Saksena S, Wahlman J, Teis D, Johnson AE, Emr SD. Functional reconstitution of ESCRT-III assembly and disassembly. Cell. 2009; 136:97–109. [PubMed: 19135892]

10. Wollert T, Wunder C, Lippincott-Schwartz J, Hurley JH. Membrane scission by the ESCRT-III complex. Nature. 2009; 458:172–177. [PubMed: 19234443]

11. Bajorek M, et al. Biochemical Analyses of Human IST1 and Its Function in Cytokinesis. Mol Biol Cell. 2009

12. Dimaano C, Jones CB, Hanono A, Curtiss M, Babst M. Ist1 regulates vps4 localization and assembly. Mol Biol Cell. 2008; 19:465–474. [PubMed: 18032582]

13. Rue SM, Mattei S, Saksena S, Emr SD. Novel ist1-did2 complex functions at a late step in multivesicular body sorting. Mol Biol Cell. 2008; 19:475–484. [PubMed: 18032584]

14. Agromayor M, et al. Essential role of hIST1 in cytokinesis. Mol Biol Cell. 2009; 20:1374–1387. [PubMed: 19129480]

15. Babst M, Katzmann D, Estepa-Sabal E, Meerloo T, Emr S. Escrt-III An endosome-associated heterooligomeric protein complex required for mvb sorting. Dev Cell. 2002; 3:271–282. [PubMed: 12194857]

16. Muziol T, et al. Structural basis for budding by the ESCRT-III factor CHMP3. Dev Cell. 2006; 10:821–830. [PubMed: 16740483]

17. Shim S, Kimpler LA, Hanson PI. Structure/function analysis of four core ESCRT-III proteins reveals common regulatory role for extreme C-terminal domain. Traffic. 2007; 8:1068–1079. [PubMed: 17547705]

18. Lata S, et al. Structural basis for autoinhibition of ESCRT-III CHMP3. J Mol Biol. 2008; 378:816–825.

19. Lin Y, Kimpler LA, Naismith TV, Lauer JM, Hanson PI. Interaction of the mammalian endosomal sorting complex required for transport (ESCRT) III protein hSnf7-1 with itself, membranes, and the AAA+ ATPase SKD1. J Biol Chem. 2005; 280:12799–12809. [PubMed: 15632132]

20. Zamborlini A, et al. Release of autoinhibition converts ESCRT-III components into potent inhibitors of HIV-1 budding. Proc Natl Acad Sci U S A. 2006; 103:19140–19145. [PubMed: 17146056]

21. Kieffer C, et al. Two distinct modes of ESCRT-III recognition are required for VPS4 functions in lysosomal protein targeting and HIV-1 budding. Dev Cell. 2008; 15:62–73. [PubMed: 18606141]

22. McCullough J, Fisher RD, Whitby FG, Sundquist WI, Hill CP. ALIX-CHMP4 interactions in the human ESCRT pathway. Proc Natl Acad Sci U S A. 2008; 105:7687–7691. [PubMed: 18511562]

23. Tsang HT, et al. A systematic analysis of human CHMP protein interactions: Additional MIT domain-containing proteins bind to multiple components of the human ESCRT III complex. Genomics. 2006; 88:333–346. [PubMed: 16730941]

24. Row PE, et al. The MIT domain of UBPY constitutes a CHMP binding and endosomal localization signal required for efficient epidermal growth factor receptor degradation. J Biol Chem. 2007; 282:30929–30937. [PubMed: 17711858]

25. Rodriguez-Galan O, Galindo A, Hervas-Aguilar A, Arst HN, Penalva MA. Physiological involvement in pH signalling of Vps24-mediated recruitment of Aspergillus PalB cysteine protease to ESCRT-III. J Biol Chem. 2008 epublication ahead of print.

26. Yorikawa C, et al. Human calpain 7/PalBH associates with a subset of ESCRT-III-related proteins in its N-terminal region and partly localizes to endocytic membrane compartments. J Biochem. 2008; 143:731–745. [PubMed: 18316332]

27. Yang D, et al. Structural basis for midbody targeting of spastin by the ESCRT-III protein CHMP1B. Nat Struct Mol Biol. 2008; 15:1278–1286. [PubMed: 18997780]

28. Stuchell-Brereton MD, et al. ESCRT-III recognition by VPS4 ATPases. Nature. 2007; 449:740–744. [PubMed: 17928862]

29. Obita T, et al. Structural basis for selective recognition of ESCRT-III by the AAA ATPase Vps4. Nature. 2007; 449:735–739. [PubMed: 17928861]

30. Samson RY, Obita T, Freund SM, Williams RL, Bell SD. A role for the ESCRT system in cell division in archaea. Science. 2008; 322:1710–1713. [PubMed: 19008417]

31. Azmi IF, et al. ESCRT-III Family Members Stimulate Vps4 ATPase Activity Directly or via Vta1. Dev Cell. 2008; 14:50–61. [PubMed: 18194652]

32. Xiao J, et al. Structural basis of Vta1 function in the multivesicular body sorting pathway. Dev Cell. 2008; 14:37–49. [PubMed: 18194651]

33. Shim S, Merrill SA, Hanson PI. Novel Interactions of ESCRT-III with LIP5 and VPS4 and their Implications for ESCRT-III Disassembly. Mol Biol Cell. 2008; 19:2661–2672. [PubMed: 18385515]

34. Welsch S, et al. Ultrastructural analysis of ESCRT proteins suggests a role for endosome-associated tubular-vesicular membranes in ESCRT function. Traffic. 2006; 7:1551–1566. [PubMed: 17014699]

35. Zwart PH, et al. Automated structure solution with the PHENIX suite. Methods Mol Biol. 2008; 426:419–435. [PubMed: 18542881]

36. DeLano, WL. The PyMOL Molecular Graphics System. Palo Alto, CA: DeLano Scientific LLC; 2008.

37. Baker NA, Sept D, Joseph S, Holst MJ, McCammon JA. Electrostatics of nanosystems: application to microtubules and the ribosome. Proc Natl Acad Sci U S A. 2001; 98:10037–10041. [PubMed: 11517324]

38. Cole JL. Analysis of heterogeneous interactions. Methods Enzymol. 2004; 384:212–232. [PubMed: 15081689]

39. Laue, T.; Shah, B.; Ridgeway, T.; Pelletier, S. Computer-aided interpretation of analytical sedimentation data for proteins. In: Rowe, A.; Horton, J., editors. Ultracentrifugation in Biochemistry and Polymer Science. Cambridge, England: Royal Society of Chemistry; 1992. p. 90-125.

40. Otwinowski, Z. Oscillation data reduction program. In: Sawyer, L.; Isaacs, N.; Bailey, S., editors. Data Collection and Processing. Warrington, UK: SERC Daresbury Laboratory; 1993. p. 56-62.

41. Terwilliger TC, Berendzen J. Automated structure solution for MIR and MAD. Acta Crystallographica. 1999; D55:849–861. [PubMed: 10089316]

42. Cowtan KD, Zhang KY. Density modification for macromolecular phase improvement. Prog Biophys Mol Biol. 1999; 72:245–270. [PubMed: 10581970]

43. Jones TA, Zou JY, Cowan SW, Kjeldgaard. Improved methods for binding protein models in electron density maps and the location of errors in these models. Acta Crystallogr A. 1991; 47(Pt 2):110–119. [PubMed: 2025413]

44. McCoy AJ, Grosse-Kunstleve RW, Storoni LC, Read RJ. Likelihood-enhanced fast translation functions. Acta Crystallogr D Biol Crystallogr. 2005; 61:458–464. [PubMed: 15805601]

45. Emsley P, Cowtan K. Coot: model-building tools for molecular graphics. Acta Crystallogr D Biol Crystallogr. 2004; 60:2126–2132. [PubMed: 15572765]

46. Murshudov GN, Vagin AA, Dodson EJ. Refinement of Macromolecular Structures by the Maximum-Likelihood Method. Acta Crystallogr D Biol Crystallogr. 1997; 53:240–255. [PubMed: 15299926]

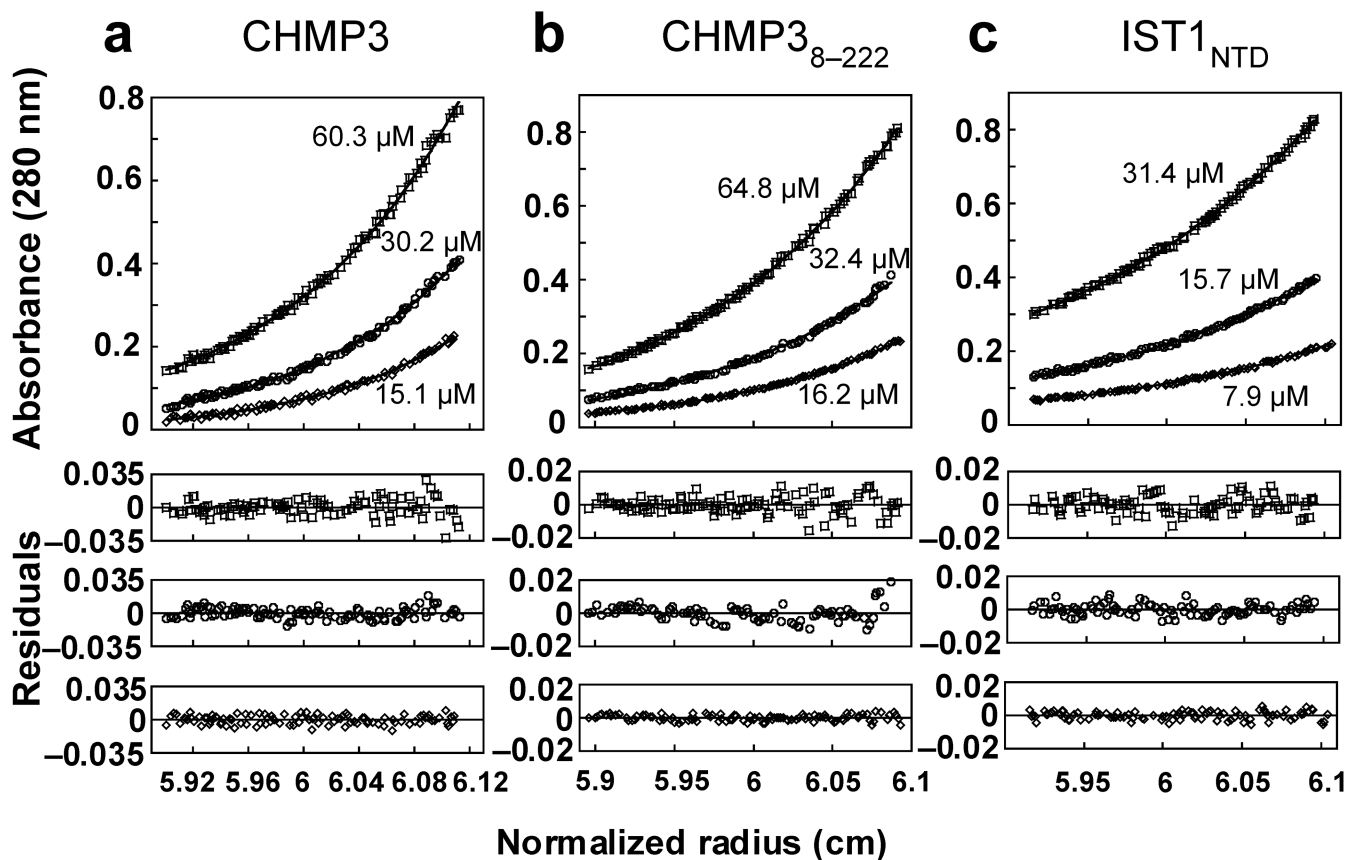47. Group CCP. The CCP4 Suite:Programs for Protein Crystallography. Acta Crystallogr D50. 1994 Nov 4.50:760–763.

Figure 1.
CHMP3, CHMP3$_{8-222}$ and IST1$_{NTD}$ are monomers in solution. Equilibrium sedimentation distributions of recombinant CHMP3 (**a**), CHMP3$_{8-222}$ (**b**), and IST1$_{NTD}$ (**c**) (upper panels), and residual differences (lower panels), with data points shown in open symbols and the single species models shown as solid lines. Rotor speeds were 20,000 RPM and initial subunit protein concentrations are shown. Data sets were also collected at 24,000 RPM (not shown) and all of the data were globally fit to single species models in which the molecular weights were allowed to float during the refinement. Estimated molecular weights were: CHMP3, 25,840 Da (MW$_{monomer}$ = 25,267 Da, M$_{obs}$/M$_{calc}$ = 1.02); CHMP3$_{8-222}$, 24,390 Da (MW$_{monomer}$ = 24,663 Da, M$_{obs}$/M$_{calc}$ = 0.99); IST1$_{NTD}$, 20,520 Da (MW$_{monomer}$ = 21,791 Da, M$_{obs}$/M$_{calc}$ = 0.94).
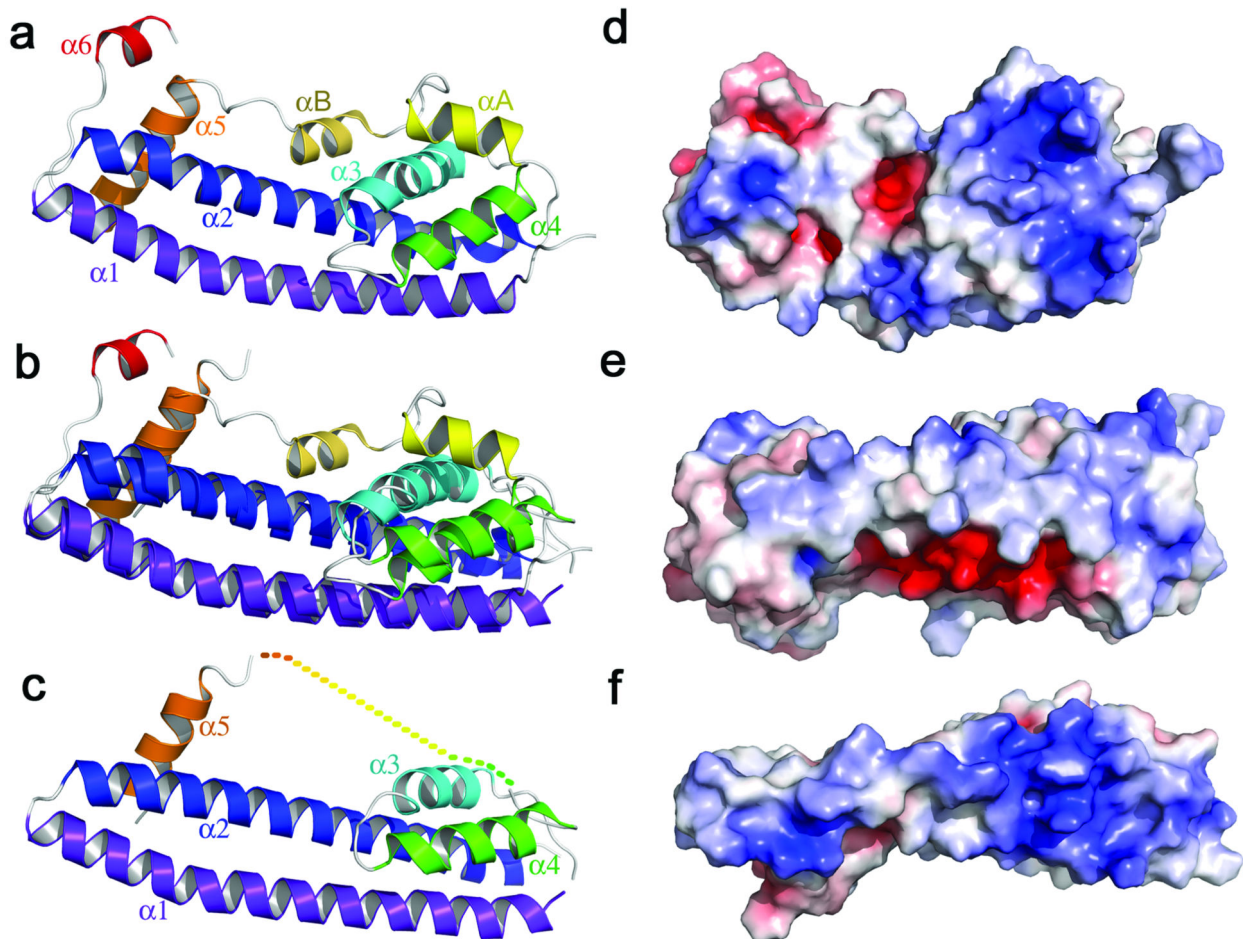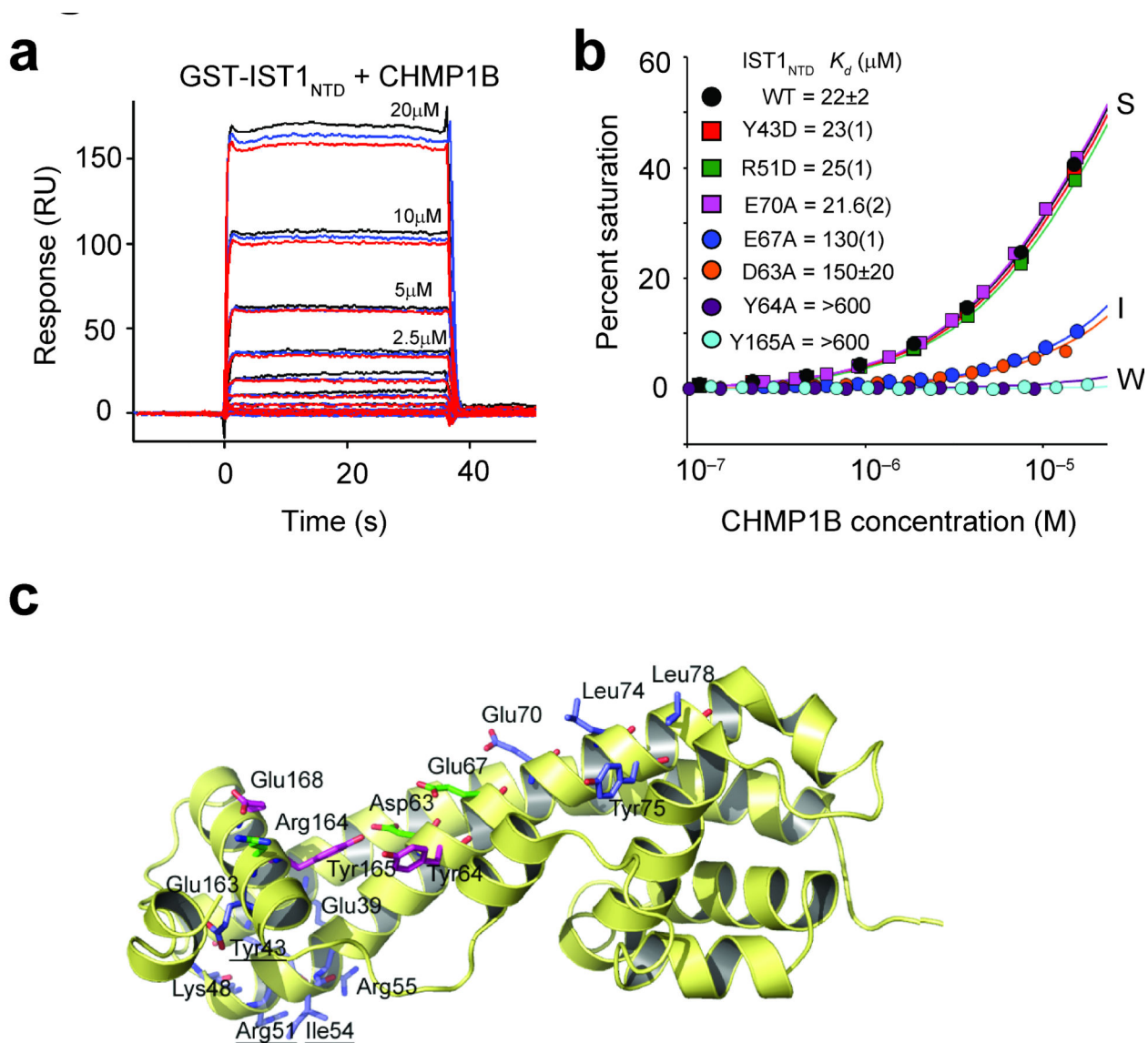
Figure 2.
Structures of IST1$_{NTD}$ and CHMP3. (**a**) Ribbon diagram and helix labeling scheme for IST1$_{NTD}$. (**b**) Overlay of the ordered regions of IST1$_{NTD}$ and CHMP3$_{8-183}$. (**c**) Ribbon diagram of CHMP3$_{8-222}$. (**d**) Space filling model of IST1$_{NTD}$, color coded to show the surface charge distribution (blue, basic; red, acidic; ± 7kV)36,37. The molecule is shown in the same orientation as in **a**. (**e**) Same as **d**. The view is toward α1, and was generated from **d** by rotation about the horizontal so that the bottom edge of **d** faces the viewer. (**f**) Space filling model of CHMP3$_{8-222}$ shown in an equivalent orientation to the view of IST1$_{NTD}$ shown in **e**, emphasizing the basicity of the α1 surface of CHMP316.
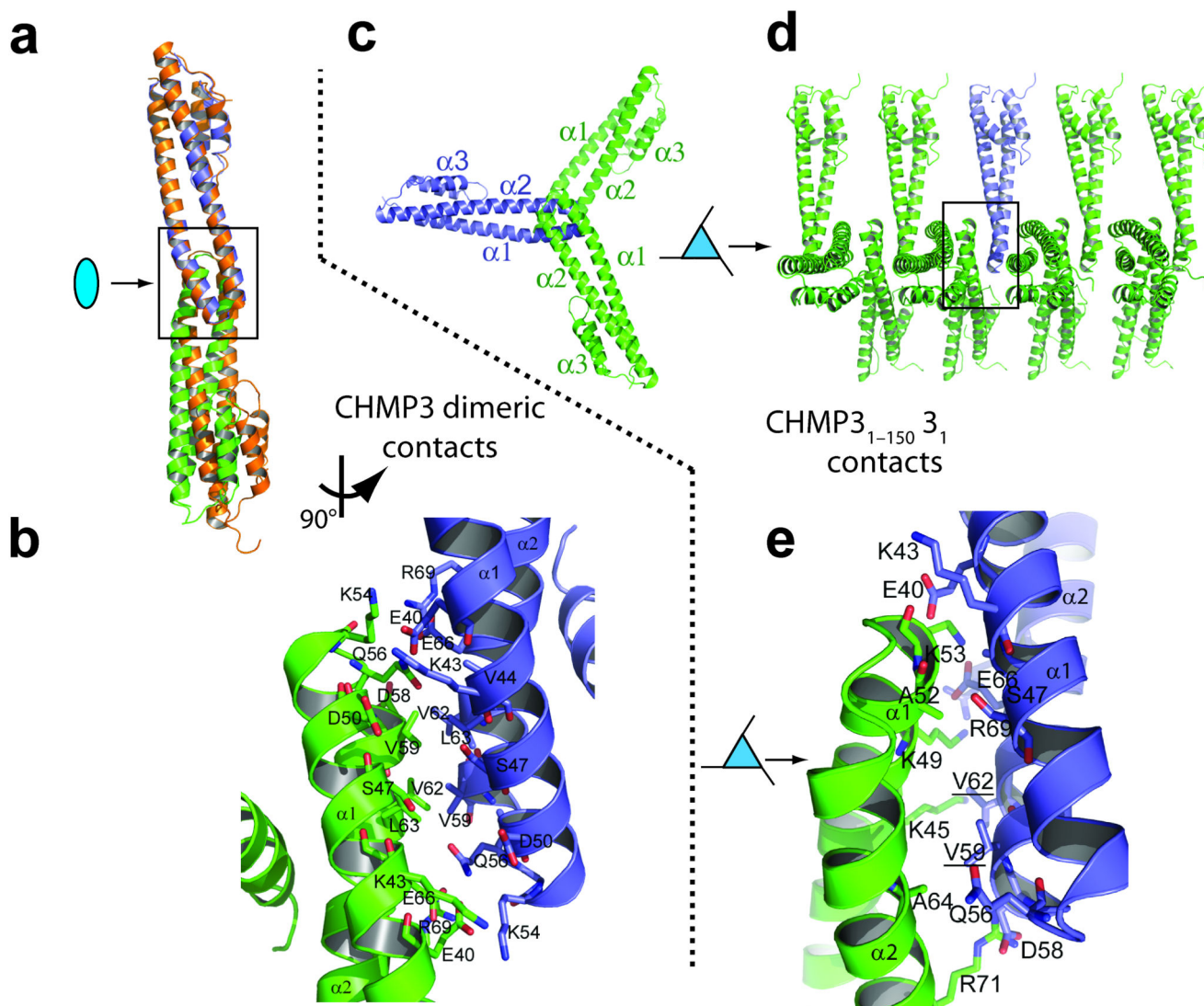
Figure 3.
CHMP3 crystal packing interactions. (**a**) Overlay of the cores of the "tip-to-tip" dimers in the crystal lattices of CHMP3$_{8–183}$ (orange)16 and CHMP3$_{8–222}$ (blue and green). The upper subunits were aligned, and the lower subunits diverge owing to small differences in their tip-to-tip interfaces. (**b**) Detailed expansion of the boxed region of CHMP3$_{8–222}$ shown in **a**. Both here and in **e**, most side chains conformations are shown as defined in the CHMP3$_{8–183}$ search model, with some minor adjustments to avoid clashes. Precise description of these side chain conformations is not possible at current resolutions. (**c**) Subunit packing down the 3_1 screw axis of the CHMP3$_{1–150}$ crystal lattice, with a single CHMP3$_{1–150}$ molecule highlighted in blue. (**d**) Same assembly as in **c**, but viewed perpendicularly to the 3_1 screw axis. (**e**) Detailed expansion of the boxed area shown in **d**.

Figure 4.

Mutational analyses of IST1-CHMP1B interactions. (**a**) Sensorgrams showing different concentrations of purified CHMP1B binding to immobilized GST-IST1$_{NTD}$. Triplicate measurements in response units (RU) are shown for each CHMP1B concentration. (**b**) Representative biosensor binding isotherms showing CHMP1B binding to wild type (WT) and mutant GST-IST1$_{NTD}$ proteins with strong (S), intermediate (I) and weak (W) binding affinities. IST1$_{NTD}$ mutations and estimated dissociation constants are given in the inset. Errors represent either standard deviations from multiple independent measurements (n 3), or standard deviations derived from single isotherms measured in triplicate (values in parentheses report the standard deviations in the final digit of the measurement).(**c**) Ribbon diagram showing the location of all IST1$_{NTD}$ mutations tested for CHMP1 binding. Mutated residues are shown explicitly, and the binding affinities of the mutant proteins are color-coded as follows: blue, strong (S) binding (binding affinities within 1.5-fold of wild type
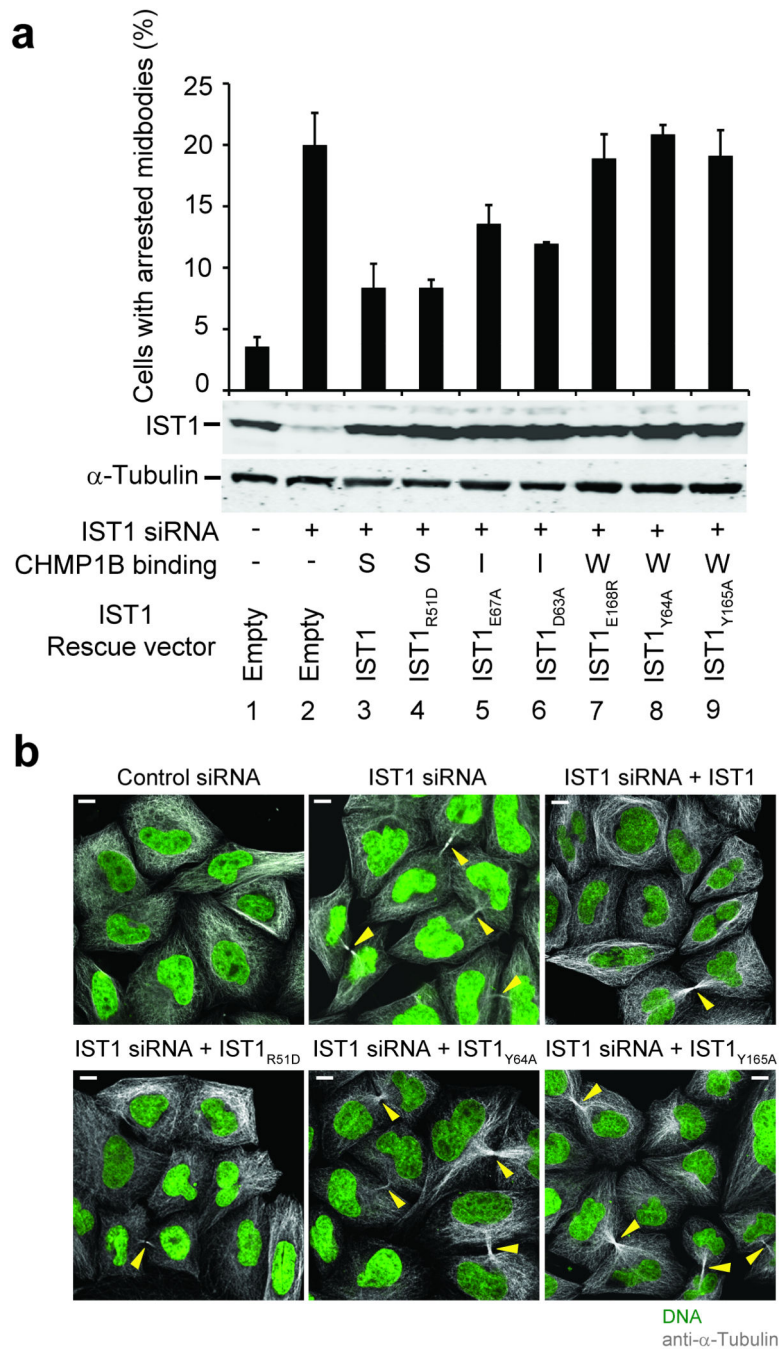
$IST1_{NTD}$); green, intermediate (I) binding (binding affinity reduced 1.5–8 fold); magenta, weak (W) binding (binding affinity reduced 8-fold).

Figure 5.
Requirement for IST1-CHMP1 interactions during abscission. (**a**) The upper panel shows quantified abscission defects as reflected in the percentages of HeLa M cells with visible midbodies following siRNA treatment to deplete endogenous IST1 (lanes 2–9) and rescue with an empty vector control (lane 2, negative control) or with vectors expressing wild type IST1 (lane 3, positive control) or the designated IST1 mutants (lanes 4–9). Untreated cells are shown in lane 1. Error bars show standard deviations from three independent repetitions of the experiment. The middle panel is a western blot (anti-IST1) showing levels of soluble

endogenous IST1 (lanes 1 and 2) or exogenously expressed IST1 proteins (lanes 3–9). The bottom panel is a western blot (anti-α-Tubulin) showing expression levels of endogenous α-Tubulin (loading control). CHMP1B binding phenotypes of the different IST1 proteins are shown below: strong (S), intermediate (I), or weak (W). (**b**) Immunofluorescence images showing the midbody phenotypes of cells from a designated subset of the experiments from **a**. Microtubules (anti-α-Tubulin, grey) and nuclei (SYTOX green) were stained for reference, and yellow arrowheads highlight midbodies. Scale bars are 10μm.
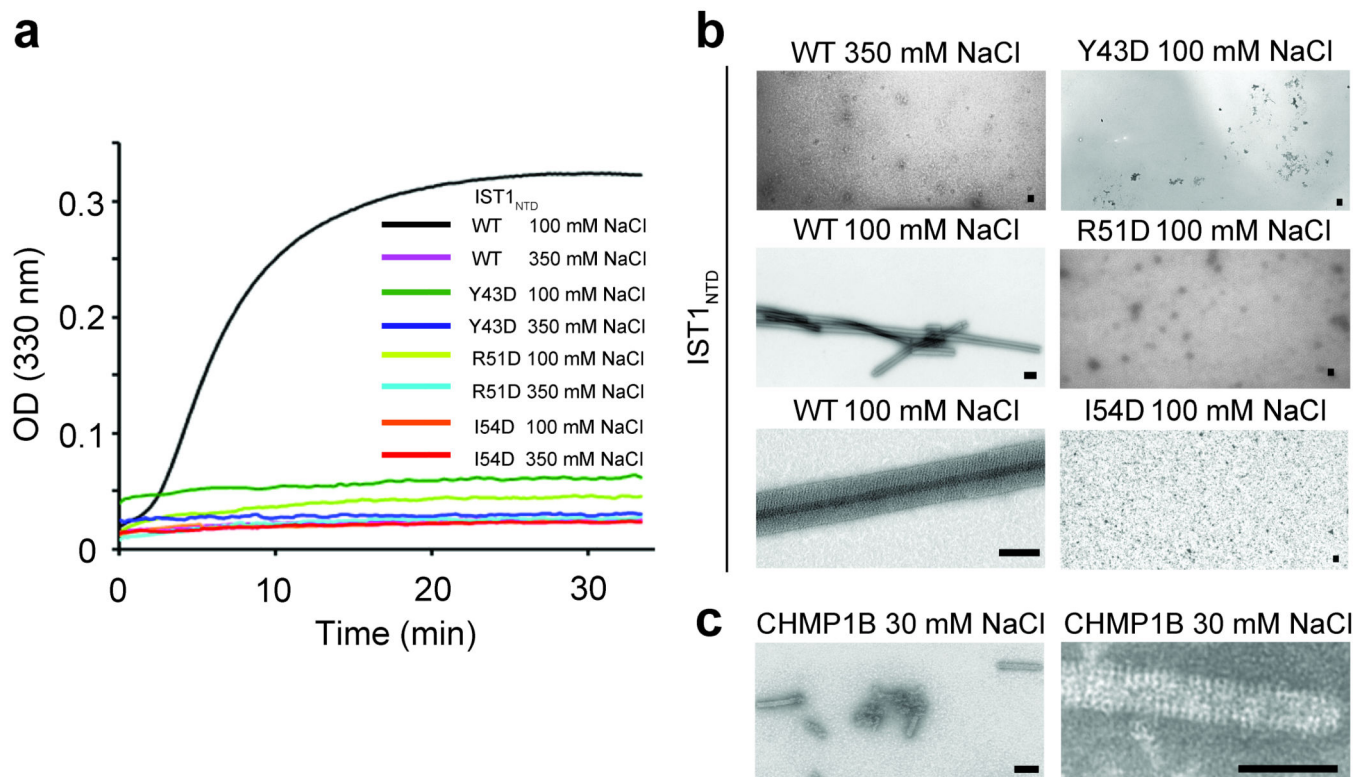
Figure 6.
IST1$_{NTD}$ and CHMP1B tube assembly. (**a**) Assembly of wild type (WT) IST1$_{NTD}$ or three different IST1$_{NTD}$ mutants with the designated amino acid substitutions at the tip of the α1/α2 hairpin (mutated residues are underlined in Fig. 4c). IST1$_{NTD}$ proteins were diluted from concentrated protein stocks in high salt buffers to final concentrations of 62 μM. Salt concentrations in the assembly buffers are provided in the inset key and protein assembly was followed by light scattering at 330 nm. (**b**) Transmission electron microscopic images of a subset of the wild type and mutant IST1$_{NTD}$ assembly reactions from **a**. Note that IST1$_{NTD}$ only assembled under low salt conditions (compare upper and middle left panels) and that IST1$_{NTD}$ proteins with different point mutations at the tip of the α1/α2 hairpin did not assemble in either high salt (not shown) or low salt conditions (right panels). An expanded view of a single IST1$_{NTD}$ tube is shown in the lower left panel. Scale bars are 500 nm. (**c**) Transmission electron microscopic images of CHMP1B tubes assembled under low salt conditions. A field of tubes is shown in the left panel and an expanded view of a single CHMP1B tube is shown in the right panel. Scale bars are 500 nm.
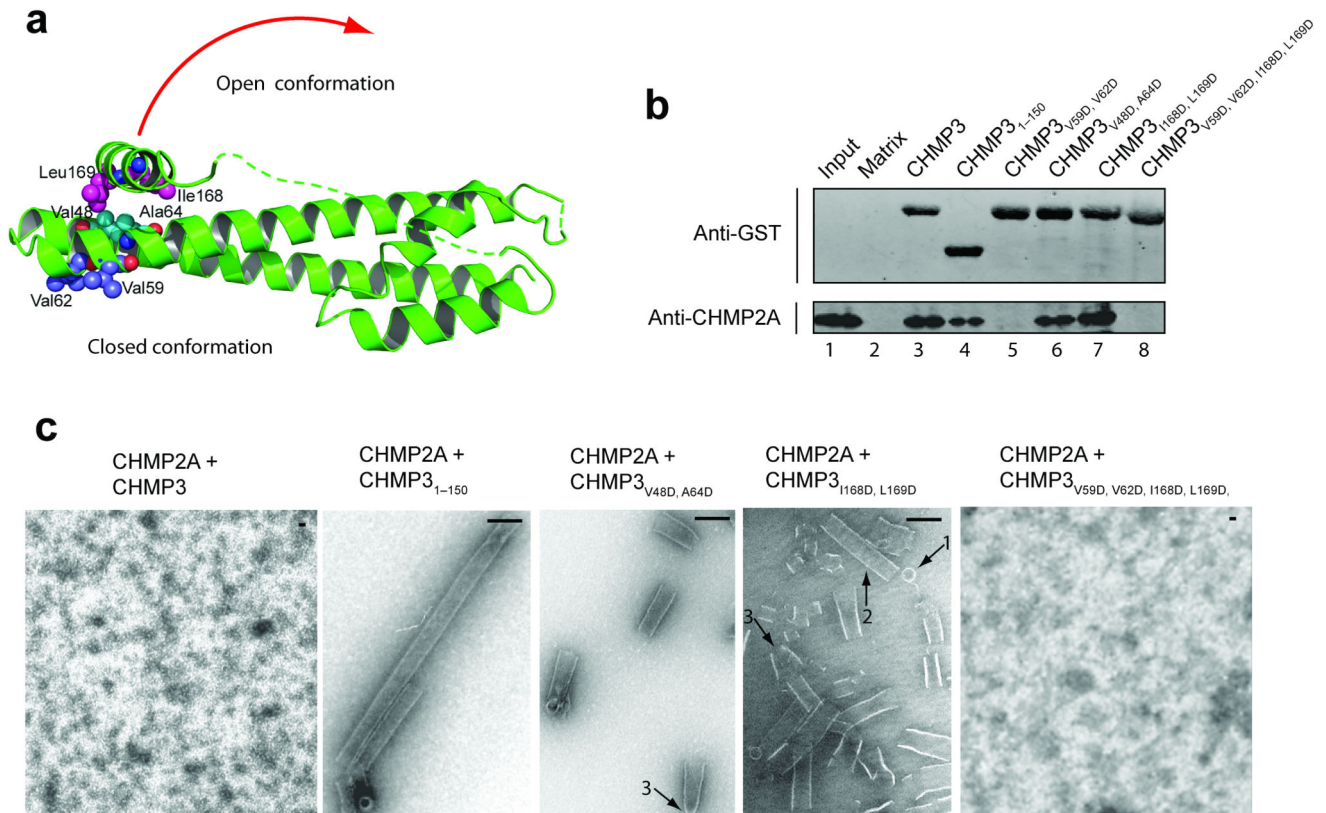
Figure 7.
CHMP3 activation *in vitro*. (**a**) Ribbon diagram showing the locations of mutated CHMP3 residues at the tip of the α1/α2 hairpin (purple) and activating mutations on either side of the interface between the core α2 helix (cyan) and the autoinhibitory α5 helix (magenta). The red arrow suggests how the closed CHMP3 conformation might convert into an open conformation by dissociation of the autoinhibitory α5 helix from the core. (**b**) GST pull-down analyses of the binary CHMP3/CHMP2A interaction. Pure recombinant CHMP2A (lower panel, anti-CHMP2A) was tested for binding to a glutathione sepharose matrix (lane 2, negative control) or to immobilized wild type (lane 3) or mutant GST-CHMP3 proteins (lanes 4–8). Both proteins were detected by Western blotting, and input CHMP2A (0.3%) is shown in lane 1 for reference. (**c**) EM analyses of helical CHMP3-CHMP2A assembly. Different panels show assemblies formed by 1:1 mixtures CHMP2A with: full length, wild type CHMP3 (panel 1, negative control, no assembly), CHMP3$_{1-150}$ core domain (panel 2, positive control), activated CHMP3$_{V48D,A64D}$ (panel 3), activated CHMP3$_{I168D,L169D}$ (panel 4), and activated and tip mutant CHMP3$_{I168D,L169D,V59D,V62D}$ (panel 5, no assemblies). Arrows highlight rings (1), tubes (2), and cones/tapered tubes (3). Scale bars are 100 nm.
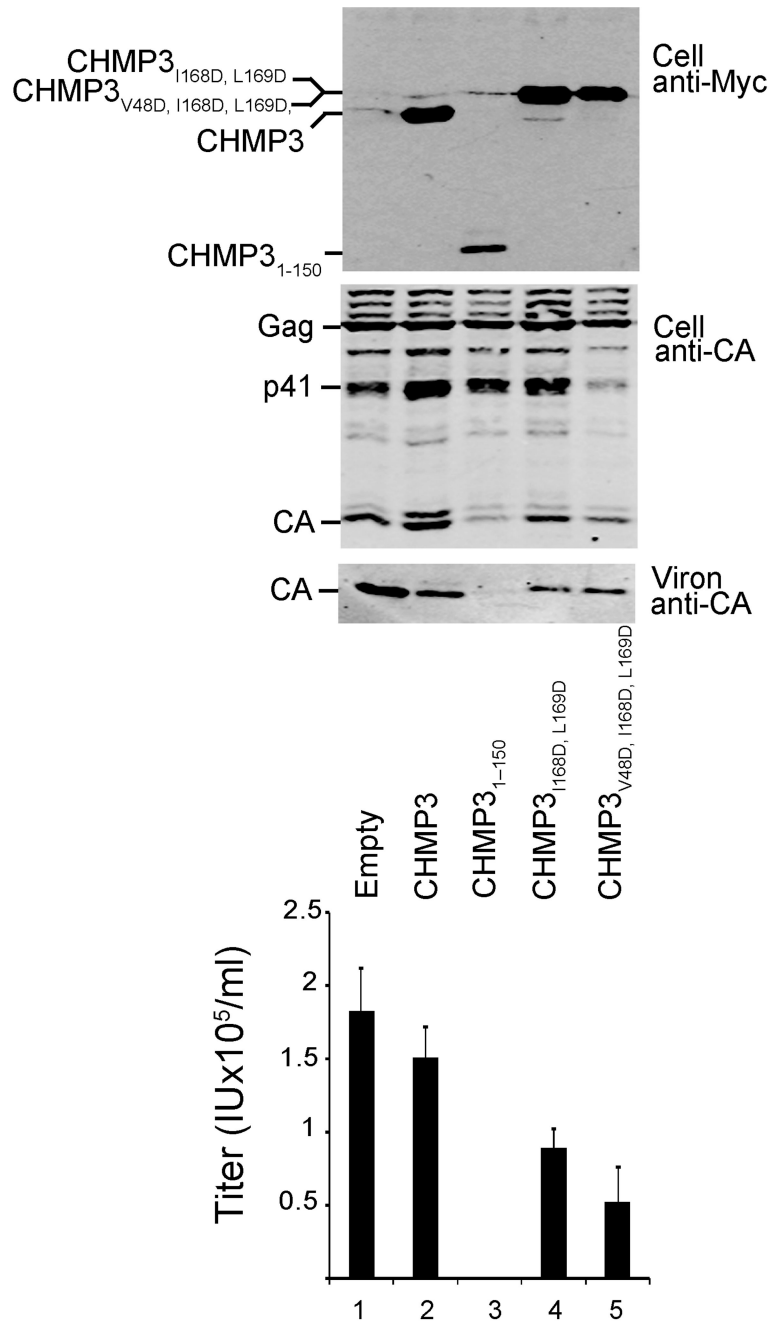
Figure 8.

CHMP3 activation *in vivo*. HIV-1 vector expression and release upon co-expression with an empty vector (negative control, lane 1), or with vectors expressing wild type CHMP3 (negative control, lane 2), a CHMP3$_{1-150}$ protein lacking the entire autoinhibitory region (positive control, lane 3), proteins with activating mutations in the α5-core interface: CHMP3$_{I168D, L169D}$ (lane 4), and CHMP3$_{V48D, 168D, L169D}$ (lane 5). Western blots in the first two panels show cellular expression levels of CHMP3-Myc proteins (panel 1, anti-Myc) and of the viral Gag protein and its p41 and CA processing products (panel 2, anti-CA). The

western blot in panel 3 shows levels of released, virion-associated CA proteins. The bottom graph shows the infectious titers of HIV-1 vectors released under the different conditions (infectious units ml^{-1}, error bars show standard deviations in multiple titer measurements, n 4).

Table 1

IST1$_{NTD}$ and CHMP3 Crystallographic Statistics

	IST1$_{NTD}$ – Native 1	IST1$_{NTD}$ – Peak 1	IST1$_{NTD}$ – Inflection 1	IST1$_{NTD}$ – Remote 1	IST1$_{NTD}$ – Native 2	CHMP3$_{8–222}$	CHMP3$_{1–150}$
Data collection							
Space group	P4$_3$2$_1$2	P4$_3$2$_1$2	P4$_3$2$_1$2	P4$_3$2$_1$2	P2$_1$	P2$_1$	P6$_1$
Cell dimensions							
a, b, c (Å)	57.2, 57.2, 157.2	57.6, 57.6, 157.1	57.6, 57.6, 157.2	57.7, 57.7, 157.3	29.3, 92.4, 33.25	36.5, 131.5, 48.5	111.5, 111.5, 30.6
α, β, γ (°)	90.0, 90.0, 90.0	90.0, 90.0, 90.0	90.0, 90.0, 90.0	90.0, 90.0, 90.0	90.0, 97.0, 90.0	90.0, 108.1, 90.0	90.0, 90.0, 120.0
Resolution (Å)	40 – 2.6 (2.7 – 2.6)	40 – 3.4 (3.5 – 3.4)	40 – 3.4 (3.5 – 3.4)	40 – 3.4 (3.5 – 3.4)	50 – 1.80 (1.86 –1.80)	50 – 4.0 (4.14 – 4.0)	25 – 3.7 (3.83-3.7)
R$_{sym}$	6.8 (34)	7.5 (16)	5.9 (15)	6.5 (14)	5.8 (15)	0.16 (15)	0.063 (55)
I / σI	13.5 (1.7)	23.9 (5.0)	24.3 (4.4)	24.4 (3.8)	19.2 (4.6)	9.3 (2.9)	18.4 (2.2)
Completeness (%)	97.7 (88.3)	88.5 (56.5)	87.7 (55.4)	83.4 (42.8)	97.2 (79.1)	78.7 (43.9)	99.2 (96.8)
Redundancy	3.8 (2.8)	6.7 (5.8)	3.9 (3.6)	3.9 (4.0)	3.1 (1.8)	4.0 (2.8)	3.2 (3.1)
Refinement							
Resolution (Å)	40 – 2.6				50 – 1.80	38 – 4.0	24 – 3.7
No. reflections	7968				15213	2936	2449
R$_{work}$ / R$_{free}$ (%)	25.9 / 29.8				19.5 / 24.7	37	41
No. atoms							
Protein	1438				1558	2274	973
Water	35				163	0	0
B-factors (Å^2)							
Protein	87.2				26.0	n/a[1]	n/a[1]
Water	69.0				39.4	n/a[1]	n/a[1]
R.m.s. deviations							
Bond lengths (Å)	0.0007				0.011	n/a[1]	n/a[1]
Bond angles (°)	1.2				1.3	n/a[1]	n/a[1]

[1] Bfactors and individual atoms were not refined and are unchanged from the molecular replacement model.